Journal Pre-proof

Active vibration control of an equipment mounting link for an exploration robot
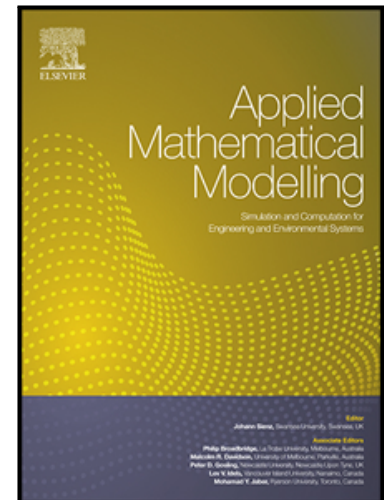
D. Williams, H. Haddad Khodaparast, S. Jiffri

Please cite this article as: D. Williams, H. Haddad Khodaparast, S. Jiffri, Active vibration control of an equipment mounting link for an exploration robot, *Applied Mathematical Modelling* (2021), doi: https://doi.org/10.1016/j.apm.2021.02.016

Highlights for review

Active vibration control of a flexible robot manipulator link

- The models provide accurate predictions of the corresponding experiments.

- The low-cost components have been proven to have good performance.

- The piezoelectric sensor yields an unconventional controlled response.

- An analytical model of only the link has been proven to be sufficient.

- The control system was proven as an effective solution against unwanted vibrations.

Active vibration control of an equipment mounting link for an exploration robot

D. Williams*, H. Haddad Khodaparast, S. Jiffri

College of Engineering, Swansea University, UK

Abstract

This research seeks a practical, reliable and effective solution to the problem of nuisance vibrations experienced within robot systems. This research suggests a potential application of a thin, lightweight camera mounting arm on a robot manipulator for use during search and rescue missions and exploration. Envisioning the robot arm mounted upon a drone or a rover vehicle, the control system will need to be both small and lightweight. The environment for such an application is likely to be dangerous, and as such the chosen components should be inexpensive and easily maintainable. Thus, components were selected whilst considering these constraints. The utilisation of piezoelectric sensors and actuators has been driven by their desirable electro-mechanical properties and their almost negligible influence on the functionality of a system. However, their inclusion within the control system, which applies control proportionally to the sensors, produced an interesting response from the closed loop system. This work builds upon previous research through the observation and understanding of this response, which proves to be more akin to proportional-derivative control. The electro-mechanically coupled analytical model of the link and surface mounted sensors/actuators, that is developed in this paper using Euler-Bernoulli Beam theory, provides insight into this unconventional response. This analytical model of the link structure in addition to a kinematic model of the robot are validated through their representation of experimental results. A compari-

---

*Corresponding author
Email address: darrenjwilliams5394@gmail.com (D. Williams)

son of the designed controlled system with a purpose-built alternative has been conducted to observe the performance of the former justifying the exchange of processing capacity for lower mass and cost. Through this comparison the effect of the control system parameters on the proportional-derivative response of the closed loop system is further explored. Finally, the effectiveness of the designed control system is observed when the link is mounted upon the manipulator for an array of excitation types.

Keywords: Active vibration control, Euler-Bernoulli, PZT sensors, PZT actuators, Raspberry Pi, robot manipulator, robot link.

2010 MSC: 00-01, 99-00

Nomenclature

A	Area	r	Superimposed rotational base displacement
a	DenavitHartenberg parameter	T	Homogeneous transformation matrix
ana	(Superscript) denotes analytical model	t	Time
C	Capacitance	v	Voltage
c	Viscous damping coefficient	W	Width
d	DenavitHartenberg parameter	w_b	Base displacement
$\bar{e}_{31}$	Effective transverse piezoelectric coefficient	w_{rel}	Relative transverse displacement
E	Young's modulus	α	DenavitHartenberg parameter
exp	(Superscript) denotes experimental results	Γ	Orientation of end effector about an axis
F_0	Forcing term	γ_v	Multiplication factor relating PZT output voltage to tip displacement
g	Base displacement	δ	Dirac delta function
H	Heaviside function	ϑ	Piezoelectric coupling term
h	Thickness	κ	Electromechanical coupling term
I	Second moment of inertia	Λ	Weighting factors in objective function
IMG	Frequency dependent damping coefficient	λ	Weights relating to γ_v
j	$\sqrt{-1}$	ρ	Density
K	Mass normalised reduced order stiffness term	Φ	DenavitHartenberg parameter
K_p	Proportional gain	ϕ	Mode shape
L	Length	χ	Mass normalised reduced order piezoelectric coupling term
lk	(Subscript) terms that relate to the link	Ψ	(Superscript) denotes active dimensions
M_t	Tip mass	ω	Angular frequency
n	Mode shape number	ω_n	Natural frequency
P	Generalised modal coordinate		
pa	(Subscript) relating to PZT actuators		
ps	(Subscript) relating to PZT sensors		
RE	Frequency dependent stiffness coefficient		
R	Resistance		
R_l	Resistive load		

1. Introduction

Robot manipulators are employed in a multitude of applications and their designs can vary greatly depending on the required task. Considering robot manipulators used in search and rescue missions, exploration and bomb disposal their components and materials are often constrained in terms of mass. With this restriction dictated by the moveable platform on which the manipulator is mounted, for search and rescue missions it could be deemed advantageous for a manipulator to be mounted on a drone. Furthermore, such missions may require the exploration of collapsed structures wherein access may be limited, and hence, may require that a camera be manoeuvred through small spaces. A potential solution to such a problem is to design or use a robot manipulator of suitable mass in conjunction with a long, slender additional link that would be suitable for exploring gaps within rubble. Due to the dangerous nature of the potential application(s) it would be beneficial for the components to be inexpensive and/or easily maintainable. The proposed geometry of the camera (or other equipment) armature leads to the disadvantage of the link being flexible and therefore subject to unwanted vibrations transversely along their length. Thus, a solution is sought to attenuate these unwanted vibrations, which does not contravene the previously described restrictions on size and mass.

Passive and active vibration control is a prevalent topic in current research, with the inclusion of smart materials being a popular choice. One such material is lead zirconate titanate (PZT) which demonstrates the piezoelectric effect; converting electrical current to physical force and vice versa, producing and using strain, respectively. Its popularity is derived from the high coefficient of the piezoelectric effect wherein a great amount of force can be achieved through relatively small dimensions of the material. Such small dimensions enable patches (cuboid with a thickness much smaller than the width and length) of the material to be surface mounted or layered between other materials with little disruption to the specifications and/or functionality of the original design. Active vibration control (AVC) and passive vibration control were considered for use within

this research, whilst utilising PZT elements. However, the latter requires the system to be tuned so that the control system's natural frequency corroborates with that of the structure. As a result, the equipment mounted on the free end of the link may not be as readily exchanged, especially if the mass of said equipment differs. Whilst this research focusses solely upon linear vibrations this choice was also dictated by future endeavours which intend to investigate the effects of this control on non-linear vibrations therefore expanding the potential application range for the proposed control system.

The use of a single board computer (SBC) within the control system meets the criteria of being both lightweight and inexpensive when compared to purpose built or more conventional research control and data acquisition systems. The control system was designed to operate independently of the equipment on which the flexible link is mounted, enabling the system to be used within a variety of applications. In addition if the link structure/control system was to be used as a camera arm, then the link structure and control system could be easily separated from the robot manipulator for the removal of the camera and use of other equipment. The Raspberry Pi 3 B+ (RPi) was deemed the most suitable SBC based on processing capacity, expense, mass and the number of connection methods for peripheral devices and other components, when compared to alternative SBCs. However, from the inclusion of a SBC in lieu of a conventional system arises the disadvantage of reduce processing capacity, which may in turn affect the performance of the system. Hence, it became prevalent that this research investigates the performance of a SBC compared to a purpose built control system.

Modelling the link analytically can be achieved through the use of Euler-Bernoulli beam theory (EBT) and is a prevalent method in existing research [1, 2, 3, 4]. Some of this research amongst others utilise PZT patches as actuators and/or sensors [5, 6, 7], and others have used PZT elements to attenuate vibrations in other structures such as a circular plate [8] and a cylindrical shell [9]. The limitations of passive control using PZT elements were explored by dell'Isola et al., wherein the performance of the system was dependent on the

resonance of the control system and structure [10]. Research on the control of a robot link through the use of piezoelectric actuators was conducted by Sun et al. [11] where a single link was driven by a servo motor. Garcia-perez et al. investigated the vibration control and trajectory tracking of flexible link robots [12] Shin and Choi [13] carried out research on a flexible two-link manipulator with two joints driven by servo motors, where two collocated piezoelectric patches were bonded to each link for the purpose of control. Qiu et al. [14] also conducted research with a similar experimental set-up, utilising self-tuning control and fuzzy neural networks to attenuate the vibrations along the links. The potential applications of an control system that utilises PZT elements is a prevalent consideration in research, which include the AVC of a camera mount system [15] and the passive control of flexible spacecraft appendages [16] among others. A number of researchers have considered the utilisation of a SBC within an AVC system including Abdollahpouri et al. [17], wherein the aim was to produce a control estimation for a cantilever beam employing a Raspberry Pi Model B. This brand of SBC was also included in research by Weber et al. [18] where, combined with reaction wheels, was used in the cancelling of vibrations experience by a cable-driven parallel robot. The combination of a Raspberry Pi and a MCP3008 ADC was employed by Mahmud et al. [19] for the purpose of structural health monitoring using PZT sensors. Chomette and Mamou-Mani [20] utilised a BeagleBone Black as an alternative SBC within an AVC system to suppress vibrations along a plate. The KUKA© iiwa 7 R800 is increasingly popular with research endeavours especially with the improvement of manipulator use in industrial applications, with an example being the research conducted on peg-hole disassembly using active compliance [21]. Many have also used this particular model in research to ascertain a method for the inverse kinematics of a redundant manipulator [22, 23, 24]. Modelling a robot manipulator using the DenavitHartenberg (D-H) convention is common within robotics research [25, 26, 27, 28].

This paper develops and validates a closed loop, electro-mechanically coupled analytical model of a flexible robot manipulator link with surface mounted PZT

sensors and actuators. A control system is designed, developed and analytically modelled, utilising practical, inexpensive, lightweight components. The governing equations of the closed loop analytical model would suggest that the control system influences the damping and stiffness of the structure, with the potential to yield results akin to a proportional-derivative controller. A purpose-built control system with different dependent parameters is employed to not only explore this concept, but to observe the performance of the designed control system and justify the selection of the SBC for its favourable specifications. To observe the performance of designed control system with regards to the suggested application the flexible link is then mounted on a KUKA© iiwa 7 R800, and a combination of the kinematic model of the manipulator and the analytical model of the link is considered. The experimental results are compared with those produced from the model to validate the latter, with the aim to provide a method to predict the response of similar systems.

2. Analytical and kinematic models

Analytical models of the link structure (including the PZT elements and a tip mass to represent a camera or other equipment), and the control system are developed within this section. These analytical models were combined and used to generate appropriate data for comparison in the experimental investigation where the robot manipulator is negated. These initial experiments evaluated the performance of the designed control system, utilising a purpose built control system as a reference of evaluation. The kinematic model of the robot manipulator is also discussed within this section, for the experimental investigation of the suitability of the system for the suggested application.

2.1. Analytical model of the link structure

The analytical model of the flexible link to be attached to the robot arm was created based upon Euler-Bernoulli beam theory (EBT). The justification for the utilisation of this theory lies within its simplicity and the suitability of the

dimensions of the link for said theory. The link has the boundary conditions of clamped-free, where the immobile end of the link (base) is located at the attachment to the shaker platform (SBC performance comparison) and the robot arm (suggested application suitability). The link will be subject to a base excitation $(w_b(y,t))$ along the plane of the common normal of its length and width for the observation of subsequent transverse motion. This base excitation is to be applied by the shaker platform/robot arm in a manner which will allow the study of the control for both harmonic and transient responses. Figure 1 illustrates analytical model of the link as a plan view (showing the thickness and length of the structural components), although it should be noted that this illustration is not to scale. The axes shown within this illustration coincide with the axes of the world frame of the robot manipulator (frame 0 in Figure 2).
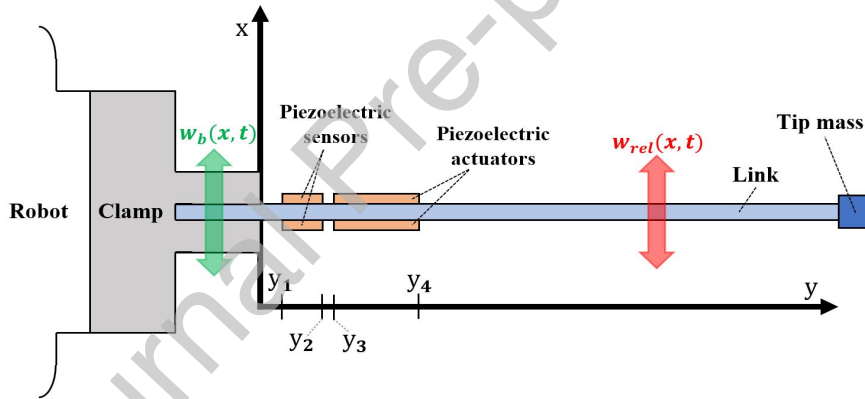

Figure 1: Illustration of analytical model.

The variables y_1 and y_2 are the start and end locations of the piezoelectric sensors, and y_3 and y_4 are the start and end locations of the piezoelectric actuators along the length of the link, respectively. The base excitation $(w_b(y,t))$ is applied along the x axis and $w_{rel}(y,t)$ represents the relative transverse motion along the length of the link. This transverse motion is parallel to the link's thickness, which is perpendicular to the ground. As the width of the link is perpendicular to the ground, the stiffness along this plane is considered great

enough to assume that gravitational effects and rotational motion are negligible. The tip mass shown in Figure 1 is included to represent the mass of a small camera, it is located at $y = L_{lk}$, where L_{lk} is the length of the link. The mass of the clamp and the shaker armature/end effector of the robot arm is not included within the link structure model as the link is considered to be perfectly clamped. The equation of motion for the structure can be written as in Equation 1.

$$
\begin{aligned}
\frac{\partial^2}{\partial y^2} &\left(EI(y)\frac{\partial^2 w_{rel}(y,t)}{\partial y^2} \right) + \rho A(y)\frac{\partial^2 w_{rel}(y,t)}{\partial t^2} \\
&\qquad\qquad\qquad\qquad +c\frac{\partial w_{rel}(y,t)}{\partial t} \\
&- \vartheta_{ps} v_{ps}(t) \left[\frac{d\delta(y-y_1)}{dy} - \frac{d\delta(y-y_2)}{dy} \right] \\
&- \vartheta_{pa} v_{pa}(t) \left[\frac{d\delta(y-y_3)}{dy} - \frac{d\delta(y-y_4)}{dy} \right] \\
&= -\left[\rho A(y) - M_t \delta(y - L_{lk}) \right] \frac{\partial^2 w_b(y,t)}{\partial t^2}
\end{aligned}
\tag{1}
$$

The inclusion of the piezoelectric actuators within the equation of motion renders the definitions as shown in Equations 2 through 4, where the former two acknowledge the alteration in stiffness and mass along the length of the link at the locations of the PZT elements. The latter (Equations 4) electromechanically couple the PZT elements and the link.

$$
\begin{aligned}
EI(y) &= E_{lk} I_{lk} + E_{ps} I_{ps} \left[H(y - y_1) - H(y - y_2) \right] \\
&\quad + E_{pa} I_{pa} \left[H(y - y_3) - H(y - y_4) \right]
\end{aligned}
\tag{2}
$$

$$
\begin{aligned}
\rho A(y) &= \rho_b A_b + \rho_{ps} A_{ps} \left[H(y - y_1) - H(y - y_2) \right] \\
&\quad + \rho_{pa} A_{pa} \left[H(y - y_3) - H(y - y_4) \right]
\end{aligned}
\tag{3}
$$

$$
\begin{aligned}
\vartheta_{ps} &= \frac{\bar{e}_{31} W_{ps}^{\Psi}}{h_{ps}} \left[\left(h_{ps} + \frac{h_{lk}}{2} \right)^2 - \frac{h_{lk}^2}{4} \right] \\
\vartheta_{pa} &= \frac{\bar{e}_{31} W_{pa}^{\Psi}}{h_{pa}} \left[\left(h_{pa} + \frac{h_{lk}}{2} \right)^2 - \frac{h_{lk}^2}{4} \right]
\end{aligned}
\tag{4}
$$

10

Note that the subscripts lk, ps and pa represent the link, piezoelectric sensor and piezoelectric actuator, respectively and the superscript Ψ represents active dimensions. E represents the Young's modulus, I the second moment of area, and ρ and A the density and the cross-sectional area, respectively. v is the voltage (output from sensors and input to actuators), M_t is the tip mass, and c is the viscous damping term. L, W and h, respectively are the length, width and thickness. The Heaviside and dirac delta functions are represented by H and δ, respectively. Lastly, $\bar{e}_{31}$ is representative of the effective transverse piezoelectric coefficient, and ϑ is the piezoelectric coupling term. It should be noted that as the voltage output from the PZT actuators are negligible in comparison to the input, the voltage output is not included in the equations. To obtain the equation of motion in terms of the generalised coordinate ($P_n(t)$) the product rule is applied to the stiffness term within Equation 1 before reducing the order of the equation. With the reduction being achieved through the substitution of the transverse motion with the series expansion in Equation 5.

$$w_{rel}\left(y,t\right) = \sum_{n=1}^{N} P_n(t)\phi_n\left(y\right) \tag{5}$$

where, $\phi_n(x)$ is the nth mode shape of the link. It should be noted that only the first mode of the link will be considered as this is the only mode that the robot arm is capable of exciting. However, the analytical model has the potential to include higher modes increasing the range of alternative applications of the model. Due to the excitation frequency limitations of the robot manipulator, the assumption of only one mode in this research may be justified. Previous research has investigated the contribution of the designed controller on higher modes, where it was concluded that no negative spill-over effects were present [29].

$$w_b(y,t) \;=\; g(t) + yr(t) \tag{6}$$

The base excitation can be expressed as in Equation 6, where $g(t)$ is the transverse base displacement and $yr(t)$ is the superimposed rotational displace-

11

ment [30]. The latter tends to zero as y tends to zero, in this case rendering the second term of Equation 6 to be zero. Dividing the remaining term by the mass and realising that for the base displacement the following relationships can be applied, where F_0 is the forcing term. This relation can additionally be utilised with the generalised coordinate (P_n) and voltage (v) terms.

$$
\begin{aligned}
g(t) &= F_0 e^{j\omega t} \\
\dot{g}(t) &= j\omega F_0 e^{j\omega t} \\
\ddot{g}(t) &= -\omega^2 F_0 e^{j\omega t}
\end{aligned}
\tag{7}
$$

enabling Equation 1 to become:

$$
\left(-\omega^2 + 2\zeta_n \omega_n j\omega + \omega_n^2\right) P_0 = F_0 + \chi_{ps} v_{ps} + \chi_{pa} v_{pa}
\tag{8}
$$

where ω represents the considered frequency range (rad/s) and ζ_n is obtained experimentally from the frequency response function (FRF) using the half-power bandwidth method. Equations 9 to 12 denote the natural frequency (ω_n), the mass normalised reduced order stiffness term (K) and the mass normalised reduced order piezoelectric coupling terms for the PZT actuators and sensors (χ), respectively.

$$
\omega_n = \sqrt{\frac{K}{\rho A(y) \int_0^{L_{lk}} \phi_n^2(y)\, dy + M_t \phi_n^2(L_{lk})}}
\tag{9}
$$

$$
K = \int_0^{L_{lk}} \left[\frac{\partial^2 EI(y)}{\partial y^2} \phi_n''(x) + 2\frac{\partial EI(y)}{\partial y} \phi_n'''(y) \right. \\
\left. + EI(y)\phi_n^{iv}(y) \right] \phi_n(y)\, dy
\tag{10}
$$

$$
\chi_{ps} = \frac{\vartheta_{ps} \int_0^{L_{lk}} \left[\frac{d\delta(y-y_1)}{dy} - \frac{d\delta(y-y_2)}{dy} \right] \phi_n(y)\, dy}{\rho A(y) \int_0^{L_{lk}} \phi_n^2(y)\, dy + M_t \phi_n^2(L_{lk})}
\tag{11}
$$

$$
\chi_{pa} = \frac{\vartheta_{pa} \int_0^{L_{lk}} \left[\frac{d\delta(y-y_1)}{dy} - \frac{d\delta(y-y_2)}{dy} \right] \phi_n(y)\, dy}{\rho A(y) \int_0^{L_{lk}} \phi_n^2(y)\, dy + M_t \phi_n^2(L_{lk})}
\tag{12}
$$

12

The governing electrical equation for the PZT sensors is stated in 13, where, respectively, C, R_l and κ_n are the capacitance, the resistive load across and the electromechanical coupling of the piezoelectric patches. This equation is coupled with Equation 8 which describes the transverse motion of the link structure.

$$\left(j\omega C_{ps} + \frac{1}{2R_{lps}}\right) v_{ps} + j\omega \sum_{n=1}^{\infty} \kappa_{nps} P_0 = 0 \tag{13}$$

2.2. Control system

The control system used within this research is a proportional controller where the voltage output from the PZT sensors is multiplied by a gain (K_p). This choice of controller was based on the consideration of the processing capability of the SBC, as well as the potential to observe the controlled response. The latter influence is based on the fact that the voltage output from the PZT sensors is dependent on the capacitance and resistance of the circuit, which lends to the controller acting in a similar manner to a proportional derivative controller. Rearranging and multiplying 13 by the complex conjugate the frequency dependent voltage output from the PZT sensors is yielded as in Equation 14, where RE and IMG represent the frequency dependent stiffness and damping coefficients, respectively.

$$v_{ps} = (-RE(\omega) - IMG(\omega)j)P_0 \tag{14}$$

where,

$$RE(\omega) = \frac{\omega^2 \, C_{ps} \, \kappa_{nps}}{\left(\omega \, C_{ps}\right)^2 + \left(1/\left(2R_{lps}\right)\right)^2} \tag{15}$$

$$IMG(\omega) = \frac{\omega \frac{1}{2R_{lps}} \kappa_{nps}}{\left(\omega \, C_{ps}\right)^2 + \left(1/\left(2R_{lps}\right)\right)^2} \tag{16}$$

subsequently, the voltage to be applied to the actuators is calculated through the use of:

$$v_{pa} = K_p v_{ps} \tag{17}$$

13

Thus, the equation of motion of the closed loop system can be written in terms of the generalised coordinate (P_0) as:

$$\frac{P_0}{F_0} = \frac{1}{-\omega^2 + (2\zeta_n\omega_n\omega + \chi_{pa}K_p IMG(\omega))\,j + \omega_n^2 + \chi_{pa}K_p RE(\omega)} \qquad (18)$$

and, utilising Equation 14 the voltage response may be written as:

$$\frac{v_{ps}}{F_0} = \frac{-RE(\omega) - IMG(\omega)j}{-\omega^2 + (2\zeta_n\omega_n\omega + \chi_{pa}K_p IMG(\omega))\,j + \omega_n^2 + \chi_{pa}K_p RE(\omega)} \qquad (19)$$

Both Equations 18 and 19 may be represented in terms of the transverse displacement through the utilisation of Equation 5.

2.3. Robot manipulator

The KUKA$^{\copyright}$ iiwa 7 R800 is analytically modelled as a seven degree of freedom robot where the Denavit-Hartenberg (D-H) parameters have been altered for simplicity and faster computation. This simplification can be observed in Figure 2 which outlines the frames on each joint as well as the D-H parameters. The image shows the arm in the pose in which all joint angles are zero and frame zero is equivalent to the world frame.

The simplification applied pertains to the D-H parameter d which is defined as the distance between the origin of the previous frame to the frame in question's x axis along the z axis of the previous frame. The joints which rotate about the z axis of the world frame have been considered to be located in the same position as the proceeding frame i.e. the origin the frames 1, 3, 5 and 7 are located at the origins of frames 2, 4, 6 and 8, respectively. Thus simplifying the model without affecting calculations [26]. The D-H parameters used in the model can be found in Table 1 along with the range of motion (ROM) and maximum joint velocity (MJV) for each joint.

In Table 1, Φ represents the angle between the joint and the previous joint about the z axis of the previous joint. a is distance between the z axis of the
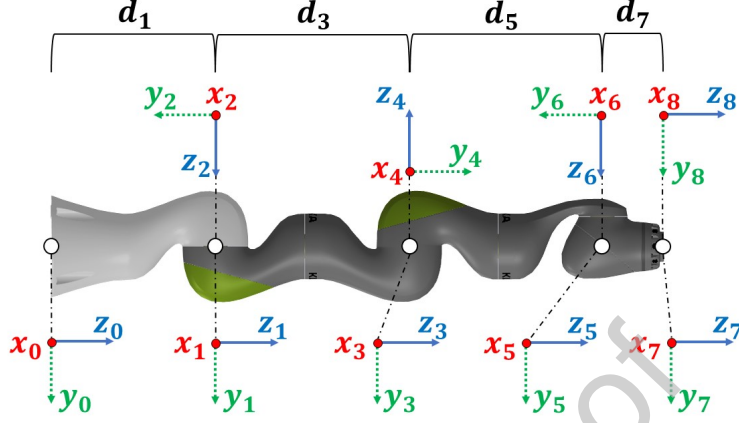
14

Figure 2: Illustration of the KUKA iiwa and its assigned coordinate frames.

joint and the previous z axis along the current x axis. α is the angle about the common normal from the previous z axis to the current z axis. Forward and inverse kinematics (FK and IK) are methods that may be used to obtain the end effector position and orientation from the joint angles and vice versa, respectively. In FK the homogeneous transformation matrix (T) is obtained using Equation 20 for each frame (i).

$$
T_{i-1}^i = \begin{bmatrix} cosine(\Phi_i) & -cosine(\alpha_i)sine(\Phi_i) & sine(\alpha_i)sine(\Phi_i) & a_i cosine(\Phi_i) \\ sine(\Phi_i) & cosine(\alpha_i)cosine(\Phi_i) & -sine(\alpha_i)cosine(\Phi_i) & a_i sine(\Phi_i) \\ 0 & sine(\alpha_i) & cosine(\alpha_i) & d_i \\ 0 & 0 & 0 & 1 \end{bmatrix}
$$
$$(20)$$

The transformation matrix for the entire robot arm from frame zero to seven is generated from the matrix multiplication of the individual frame matrices, as in Equation 21.

$$
T_0^n = T_0^1 T_1^2 T_2^3 ... T_{n-1}^n
$$
$$(21)$$

From the transformation matrix representing the end effector, the Cartesian coordinates (x,y and z) and the orientation $(\Gamma_x, \Gamma_y, \Gamma_z)$ can be extracted. The

15

Joint	Φ_j	d_j	a_j	α_j	ROM	MJV
(j)	(rad)	(m)	(m)	(rad)	($\pm$deg)	($^\circ$/s)
1	Φ_1	0.34	0	$-\pi/2$	170	98
2	Φ_2	0	0	$\pi/2$	120	98
3	Φ_3	0.4	0	$\pi/2$	170	100
4	Φ_4	0	0	$-\pi/2$	120	130
5	Φ_5	0.4	0	$-\pi/2$	170	140
6	Φ_6	0	0	$\pi/2$	120	180
7	Φ_7	0.126	0	0	175	180

Table 1: D-H parameters, range of motion (ROM) and maximum joint velocities (MJV) used in the analytical model [31].

Cartesian coordinates are found in the first three rows within last column of T_0^n and the first three columns represent the rotation matrix. Dependent on the value of the first variable within the rotation matrix, one of Equations 22 and 23 can be used to obtain the orientation. If the initial value (Γ_{11}) has a magnitude of one then Equation 22 is to be used, for any other value it is necessary to utilise Equation 23.

$$
\begin{aligned}
\Gamma_x &= 0 \\
\Gamma_y &= -\text{atan2}(\Gamma_{13}, \Gamma_{34}) \\
\Gamma_z &= 0
\end{aligned}
\tag{22}
$$

$$
\begin{aligned}
\Gamma_x &= \text{asin}(\Gamma_{21}) \\
\Gamma_y &= -\text{atan2}(\Gamma_{31}, \Gamma_{11}) \\
\Gamma_z &= \text{atan2}(\Gamma_{23}, \Gamma_{22})
\end{aligned}
\tag{23}
$$

To render the joint angles from the Cartesian coordinates and orientation requires a complex analytical solution in the instance of a system with seven degrees of freedom. Many researchers are producing methods to this complex problem, but as this research focusses on vibration control the calculation of the IK will be performed by the KUKA$^\copyright$ Sunrise software, simplifying the analytical

16

model to solely FK.

3. Experimental investigations

3.1. SBC performance evaluation

To evaluate the performance of the SBC a comparison was made with the performance of a purpose built system, the dSPACE MicroLabBox$^©$ (dSPACE). This comparison is poignant as the dSPACE is 300 times more expensive (approximately) than the RPi, and has much larger dimensions (0.31 m × 0.25 m × 0.115 m) compared to the RPi (0.0856 m × 0.0565 m × 0.017 m). To ensure that the comparison is unencumbered by the inclusion of the robot manipulator an APS 113 ELECTRO-SEIS$^®$ Long Stroke Shaker amplified through an APS 125 Power Amplifier was used to provide the base excitation. The source of excitation was used for both control systems, as well as two ZX2LD100 laser displacement sensors (LDSs) that were used to measure the traverse displacement experienced at the base and free end of the link.

The dimensions of the link were dictated by the capabilities of the robot manipulator in terms of its excitation frequency range, as the same link structure was to be used in the proceeding experiments. The frequency range of the robot manipulator was found to be 1.5 Hz to 6.75 Hz. Thus, along with the inclusion of a tip mass equal to 0.012 kg (based on the average mass of suitable cameras) and the four PZT elements, the dimensions of the link were selected to be those as outlined in Table 2. The natural frequency of the link structure was found to be 3.59 Hz, which lies comfortably within the excitation frequency range of the robot manipulator.

Figure 3 shows the set-up utilised to yield the results for both the uncontrolled and controlled vibrations along the length of the link. Where the labels used within the figure are as follows:

1. Raspberry Pi 3 B+ (RPi).
2. Analogue to digital converter (ADC).
3. High voltage drivers (HVDs).

17

Parameters	Link (Aluminium)	Piezoelectric Sensor (PZT-5A)	Piezoelectric Actuator (PZT-5A)
Overall length (m)	0.272	0.016	0.066
Overall width (m)	0.0397	0.016	0.031
Thickness (m)	0.0004	0.0003	0.0003
Active length (m)	-	0.007	0.056
Active width (m)	-	0.014	0.028
Density (kg/m^3)	2700	5440	5440
Young's Modulus (GPa)	70	60.48	60.48
Piezoelectric coefficient, $\bar{e}_{31}$	-	-11.6	-11.6
Electromechanical coupling term, κ	-	0.34	0.34
Capacitance (nF)	-	7.89	113.06

Table 2: Geometric, mechanical and electric properties of link and piezoelectric patches [32, 33].

4. Collocated piezoelectric sensors.

5. Collocated piezoelectric actuators.

6. Laser displacement sensor.

It should be noted that this image (Figure 3) has been simplified so as to better highlight the RPi system, and the reference LDS is located behind the shaker. Unfortunately, even though the RPi boasts desirable specifications including processing capacity and cost (compared to other SBCs), it suffers from some limitations, and as a result some compensations have been necessary. The RPi is incapable of reading analogue inputs, hence an analogue to digital converter (ADC) was employed. The MCP3008 is an ADC which meets the overall requirements of the control system relating to expense and mass. It has a sampling rate of approximately 1.5 kHz, and costs considerably less than alternatives on the market. However, as with the majority of its alternates the MCP3008 can only read voltages between 0V and 5V, and therefore the alternating voltage producing PZT sensors (± 8 V within this experimental
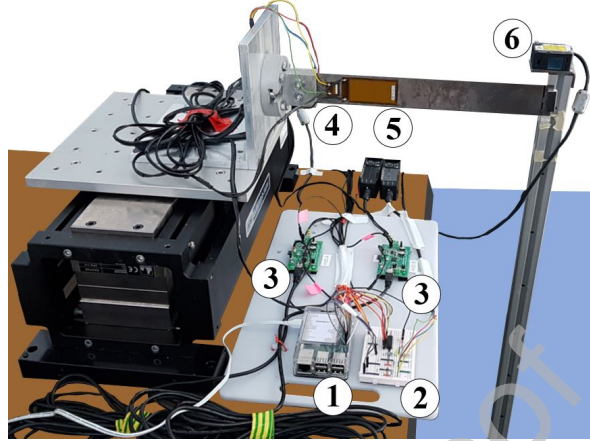
Figure 3: Simplified image of the set-up used to obtain the results for both the controlled and uncontrolled link excitations.

study) cannot be directly connected to the ADC. Therefore, a half wave rectifier circuit (HWRC) and a potential divider circuit (PDC) were employed to prevent negative voltages and voltages greater than 5V from entering the ADC for each sensor, respectively. The HWRC contains a 1N4148 diode and a 10 MΩ resistor (R_1), and the PDC is comprised of two 10 MΩ resistors (R_1 and R_2), as shown in Figure 4 for one sensor/actuator pair. It should be noted that the voltage readings obtained by the RPi are adjusted to account for the effects of the PDC and forward voltage drop of the diode.

The dSPACE does not share the same disadvantages, it is capable of reading bipolar analogue signals of $\pm 10V$. Hence, the PZT elements may be directly connected to this purpose built control system in this situation, replacing all components bar the high voltage drivers (HVDs) in Figure 4. A HVD is required for each PZT actuator as the operating voltage range of the PZT actuators is -60 V to 360 V. Whereas the maximum positive output voltage (via Pulse Width Modulation (PWM)) from the RPi is +3.3 V, and the maximum positive output voltage from the dSPACE is +10 V, hence the employment of two high voltage drivers (HVDs) (DRV2700EVM-HV500) is essential. These HVDs are capable of amplifying the signal from the RPi/dSPACE to +500 V, however due to the
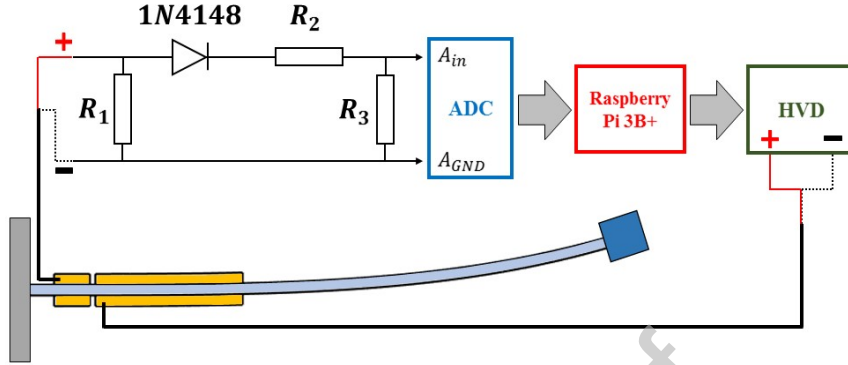
Figure 4: Illustration of the electronic circuits and the voltage manipulation which occurs as a result of the system.

operating voltage of the PZT actuators the maximum voltage will be limited to +350 V, allowing for any unexpected excess voltage from the HVDs. As the HVDs are not capable of producing negative voltages each PZT actuator was operated in the range of 0 V to 350 V. The outputs from the sensors read by the RPi were multiplied by the proportional gain (K_p), and this value was applied to the actuator on the opposing side of the link, as illustrated in Figure 4.

Two methods were utilised to evaluate the performance of the SBC; the first of which simulates the removal or reduction of base excitation, which is appropriate should the structure be travelling by land or upon a drone prior to reaching its intended destination. To simulate this motion the link structure was subjected to a sinusoidal base excitation at its natural frequency (3.59 Hz) before instantaneously stopping the excitation and applying control. The control gain K_p was increased incrementally, and the time at which the amplitude of the error between the tip and base displacements was less than 0.00035 m was taken to be the settling time. Figure 5 contains the results of this first comparative test of both the RPi and dSPACE© systems. As can be seen from the results the uncontrolled settling time is approximately 22.7 seconds, and both systems are capable of reducing the settling time to approximately 2.3 seconds. Both sets of results converge to this time which implies that increasing the gain will not

20

cause any further reduction in settling time. The main difference between the two sets of results is that gain at which the lowest settling time is achieved, the RPi system attains the lowest settling time at $K_p = 120$, whereas the dSPACE© requires a gain of $K_p = 360$ to achieve the same.
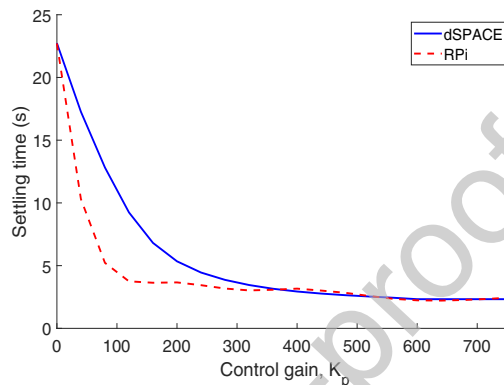

Figure 5: Comparison of the settling time achieved with increasing proportional gain between the dSPACE© and RPi systems.

The cause of this difference is best identified through the observation of the frequency response function (FRF) of the link with three different values of K_p. Figure 6 depicts the influence upon the response of the link by the two control systems across a frequency range of 1.5 Hz to 6.75 Hz. The RPi controlled results ($K_p = 240$ and $K_p = 640$) have a clear shift in frequency which is quintessentially proportional control, whereas the dSPACE results of the same gain magnitudes tend towards a derivative control trend. However, neither exclusively conform to either type of control, with the RPi also reducing the magnitude, and the dSPACE showing a subtle (by comparison to the RPi) increase to the natural frequency. Although in both cases the control is applied proportionally to the voltage from the PZT sensors, it can be seen from Equations 13 and 17 that the voltage output contains both a derivative and proportional term. Which of these terms is more dominant is governed by the resistive load and capacitance in the former equation. The form of control tends to proportional or to derivative as the resistive load increases or decreases, respectively, suggesting

21

that the two systems have different internal capacitance/resistance. However, even with this difference both systems can be observed to reduce the magnitude by the same amount at the natural frequency, evidenced by comparing the results with the vertical dashed line located at ω_n.
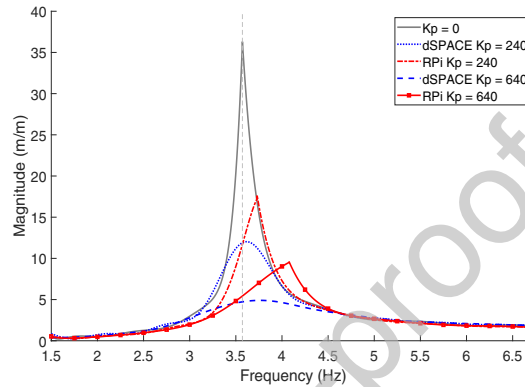

Figure 6: Comparison between the FRFs of the RPi and dSPACE control systems for different cases of gains.

The second method to compare the two systems also illustrates the most appropriate control gain. Again, the link was excited at its natural frequency, however in this case the excitation remained as the control was applied. The amplitude of the error between the tip and base displacements was recorded for a range of proportional gains. The percentage decrease was calculated based on the uncontrolled amplitude of the error.

The results of this second method are displayed in Figure 7, it can be seen that aside from some minor discrepancies at certain gain values the results match very closely. Both systems achieve a percentage decrease of approximately 89.9% at $K_p = 1040$. Higher values of gains were tested for both systems, but when $K_p > 1040$ the results between the systems differ: the percentage decrease from the RPi system increases, and from the dSPACE© system it decreases before both results converge at $K_p = 3040$ to a percentage decrease of 85.4%. Due to the difference in results and that the convergence occurs at a lower percentage decrease than that achieved when $K_p = 1040$, in an empirical manner this value
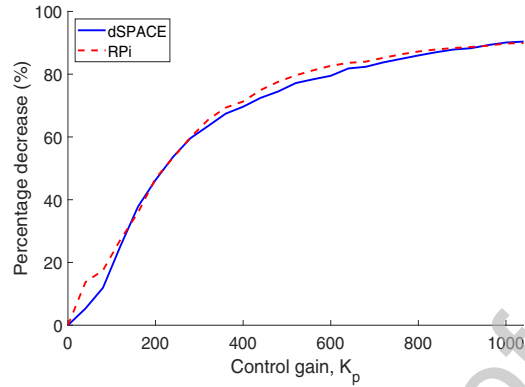
Figure 7: Comparison of the percentage decrease of tip displacement achieved with increasing proportional gain between the dSPACE© and RPi systems.

may be considered as that which produces the highest level of performance. The discrepancy between the results, at a gain higher than the optimal, can be attributed to a slight, unavoidable difference between the voltage readings from the two systems. In both cases the convergence is a result of the maximum voltage which can be applied to the PZT actuators.

From both tests it is clear that the RPi system is capable of preforming to the same standard as the dSPACE system suggesting it is a suitable, less expensive, lightweight solution to the attenuation of vibration in the robot link.

3.2. Link structure analytical model validation

The coupled analytical models of the link structure and designed control system were validated against experimental results. The experimental data was obtained through applying a swept sine motion of varying frequency (1.5 Hz to 6.75 Hz) to the base of the link. Four cases of control gain were considered in this validation ($K_p = 0$, 250, 520 and 1040), and for each case the transverse tip and base displacements along with the voltage outputs from the PZT elements were recorded. The largest gain value of these cases was selected based on the results of the prior experiments, wherein $K_p = 1040$ was empirically found to provide the largest percentage decrease (Figure 7).
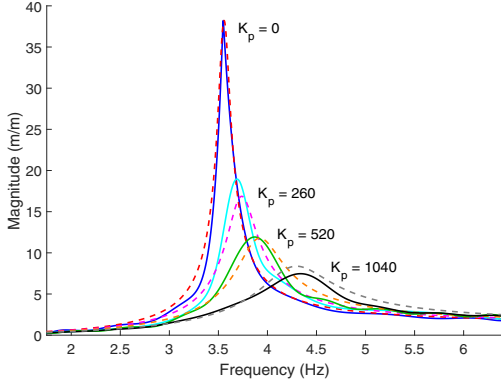
Figure 8: FRF of tip displacement divided by base displacement for multiple gains for the experimental (solid lines) and analytical (dashed lines) results.
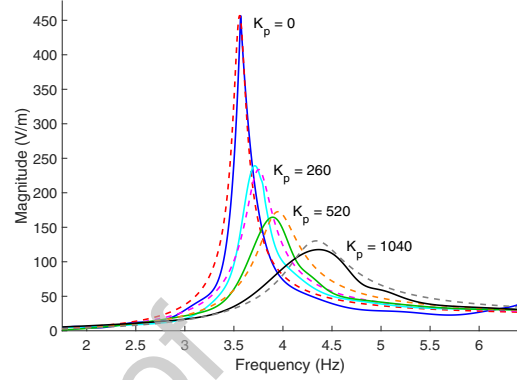
Figure 9: FRF of voltage output from PZT sensors divided by base displacement for multiple gains for the experimental (solid lines) and analytical (dashed lines) results.

Figure 8 shows the experimental (solid lines) and analytical results (dashed lines) of the FRF of the link at $K_p = 0$, 260, 520 and 1040. The magnitude of the results is the tip displacement divided by the base displacement, and as can be observed this magnitude is greatly attenuated at the optimal gain for the frequencies surrounding ω_n. For the frequencies lower and higher than this section the magnitude is not significantly affected. Considering the high decrease of magnitude at the natural frequency this negligible effect on the surrounding frequencies is deemed acceptable.

When $K_p = 0$, i.e. no control is applied to the system, the voltage output from the PZT sensors is directly proportional to the displacement experienced at the free end of the link such that $W_{rel}(L_{lk}, t) = \gamma_v v_{ps}$, where $\gamma_v = 0.0837$. However, applying control to the system reduces the displacement at the free end of the link, and disproportionally reduces the voltage output from the PZT sensors. This phenomenon is a result of the control system affecting the properties of the structure in terms of its stiffness (K) and damping ratio (ζ) and lends to a varying value of γ_v in accordance with K_p.

From Figure 10 it can be observed that the relationship between the multiplication factor (γ_v) and the proportional gain (K_p) is linear. As this variation
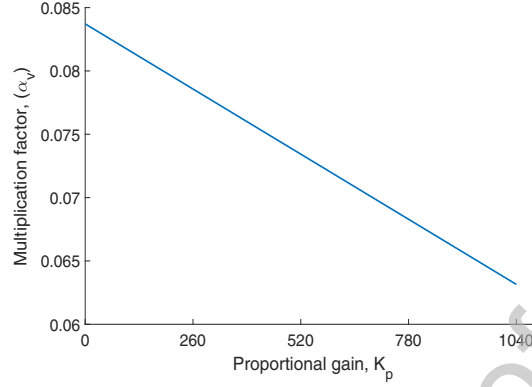
24

Figure 10: Proportionality between tip displacement and voltage output from piezoelectric sensors for varying gains.

only concerns the closed loop system in terms of the voltage output Equation 18 remains unaffected, whereas Equation 19 should be adjusted to include γ_v. Weights were introduced to adjust the influence of the $RE(\omega)$ and $IMG(\omega)$ terms (see Equations 15 and 16) such that Equation 19 becomes Equation 24.

$$\frac{v_{ps}}{F_0} = \frac{\lambda_{RE}RE(\omega) + \lambda_{IMG}IMG(\omega)j}{-\omega^2 + (2\zeta_n\omega_n\omega + \chi_{pa}K_p\lambda_{IMG}IMG(\omega))\,j + \omega_n^2 + \chi_{pa}K_p\lambda_{RE}RE(\omega)} \tag{24}$$

where, through optimisation, λ_{RE} and λ_{IMG} (the weights applied to $RE(\omega)$ and $IMG(\omega)$) were found to be 1.1 and 0.8, respectively.

It is noticeable from Figures 8 and 9 that the control system not only attenuates the vibration, but increases the natural frequency in addition. This is indicative of both proportional and derivative control, as previously this can be explained through Equations 13 and 17. With this combination of control it is clear that the RPi system is highly capable of attenuating the transverse vibration experienced along the link to a very acceptable degree.

The analytical results appear to be a good prediction of the experimental results for all cases of gain ($K_p = 0$, 260, 520 and 1040). It should be noted that adjustments were made to the PZT sensor's capacitance (C_{ps}) (see Table 2) and

resistance values (R_{lps}). An optimisation of these values was conducted where the objective function (O) was a combination of the damping and frequency of the experimental results (Equation 25).

$$O = \Lambda_1 \left(\frac{\omega_n^{ana}}{\omega_n^{exp}} - 1 \right)^2 + \Lambda_2 \left(\frac{\zeta_n^{ana}}{\zeta_n^{exp}} - 1 \right)^2 \tag{25}$$

where the superscripts *ana* and *exp* denote the analytical and experimental results, respectively. Λ_1 and Λ_2, are weights within the function and were respectively set to 0.9 and 0.1. Utilising the optimisation method yielded: $C_{ps} = 0.01$ Farads and $R_{lps} = 2.88$ Ohms.

Although the circuit diagram in Figure 4 would suggest that $R_{lps} = 15\ M\Omega$, the RPi compensates for this resistance through the manipulation of the input voltage such that the gain is applied to a voltage magnitude equivalent to that produced by the PZT sensors. Thus, the resistors within the circuit should be negated in the analytical model as the RPi masks their function, leaving only a small value of resistance found within the wires and other components. To some extent this manipulation of voltage would also affect the value of capacitance required in the analytical model. However it is more likely to be the contribution of capacitance elsewhere in the circuit (i.e. the RPi, the MCP3008 and the diodes) which lends to an increase of the capacitance stated in Table 2.

3.3. Suggested application suitability

With the RPi showing a promising level of performance, especially in comparison to a purpose built control system, its suitability for use in the suggested application required further confirmation. The excitation source used in the performance evaluation is only capable of one dimensional excitation, whereas a robot manipulator will provide three dimensional excitation which highlights the prevalence of this experimental study. The link was subjected to two types of motion, with the first being an impulse motion where the first joint of the robot manipulator was moved $10°$ at its maximum velocity of $98°/s$, with the aim to reduce the resultant settling time. The second type of motion consisted of the link being excited harmonically at its natural frequency (3.59 Hz), with

the intention for the control system to reduce the magnitude of the voltage output from the PZT sensors. Both of these types of motion were chosen based on the likelihood of the link structure experiencing similar excitations during its use within the suggested application. The decision to utilise the voltage output as a method of monitoring the vibrations experienced by the link was driven by the impracticalities that would have arisen through the employment of the LDSs. Utilising this monitoring method was found to provide a good indication of the vibration attention as presented in section 3.2.
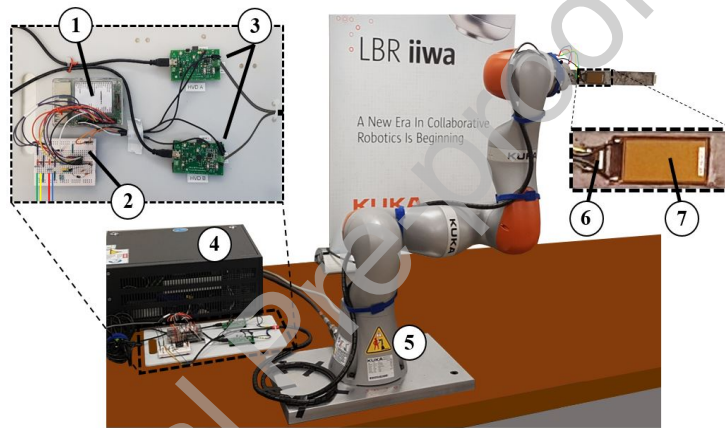

Figure 11: Image of the experimental set-up of the flexible link mounted upon the KUKA$^{\copyright}$ manipulator.

Figure 11 illustrates the experimental set-up of the flexible link mounted on the end effector of the KUKA$^{\copyright}$ iiwa 7 R800. The components are numbered as follows:

1. Raspberry Pi 3B+.

2. ADC, HWRC and PDC.

3. High voltage drivers.

4. KUKA$^{\copyright}$ Sunrise Cabinet robot controller.

5. KUKA$^{\copyright}$ iiwa 7 R800 manipulator.

6. Collocated piezoelectric sensors.

27

7. Collocated piezoelectric actuators.

Figure 12 shows the results of the control system's impact upon the transient response. The data proves that the RPi system is capable of effectively reducing the settling time of the link when it is subjected to an impulse-like motion. With no control ($K_p = 0$) the settling time to achieve a voltage of zero volts is approximately 9.04 s, this is reduced to approximately 2.76 s at a proportional gain (K_p) of 340. It is at this point the settling time converges and increasing the value of K_p causes no further reduction in settling time.
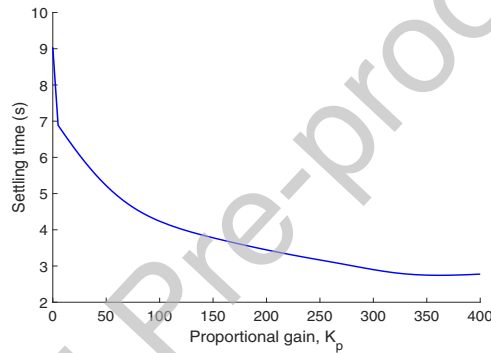

Figure 12: Settling time against proportional gain (K_p) for joint one of the KUKA© moving 10° at 100% velocity.

The second type of motion (harmonic at the natural frequency of the link) was achieved through a circular motion of the end effector. Moving the end effector in a sinusoidal manner was deemed impractical for this investigation. The results of this motion produced an ill form of a sine wave, with a delay at the extremes of the motion. This was due to the physical system being incapable of instantaneously altering the direction of the motors within the joints. Hence a circle was utilised wherein a cosine wave was attained along the z axis of the world frame of the robot manipulator (frame 0 in Figure 2), and a sine motion along the x. The latter axis is parallel to the axis in which the excitation was applied in previous experimental studies (i.e. the x axis in Figure 1). As the z axis is parallel to the width of the link structure, the stiffness in this direction

28

is deemed adequately sufficient so that the rotational effects of the motion may be deemed negligible. Thus, the previously developed analytical model may be employed where it is assumed that motion only occurs along the x axis. The required radius and velocity of the circular motion for each frequency in the range 1.5 Hz to 6.75 Hz was found, ensuring that the centripetal acceleration remained constant. For the natural frequency of the link structure, the radius was set to be 0.0015 m and the velocity of the joints was set to 5% of their maximum.
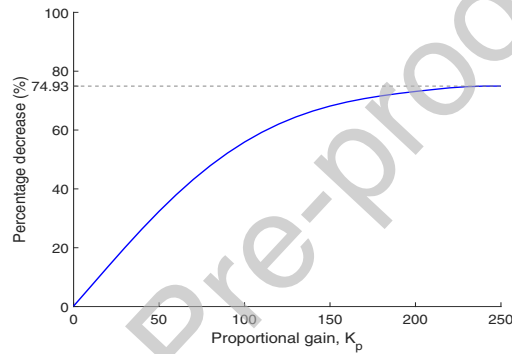

Figure 13: Percentage decrease of voltage from sensors when excited at the natural frequency, when mounted on the KUKA$^{©}$ manipulator.

Figure 13 contains the results of this experiment, where the gain value (K_p) is increased incrementally. The percentage decrease is calculated from the amplitude of the voltage output from the PZT sensors when no control is applied. It can be observed that the maximum percentage increase of 74.93% is obtained at $K_p = 200$, after which a convergence of the percentage decrease occurs. This convergence suggests that the maximum allowable voltage applied to the PZT actuators has be reached, and that increasing the gain value further would not provide a further reduction of the vibration magnitude. A very noticeable difference between the results from this experimental study and those obtained in the performance evaluation of the SBC is observed (see Figure 7); the gain value at which the maximum percentage decrease occurs differs greatly. This

29

discrepancy between these gain values of the two similar experiments is a result of the difference in the acceleration of the excitation applied to the link. A larger gain in the first experiment suggests that the acceleration to which the link was subjected by the shaker is smaller, hence produces smaller voltages across the PZT sensors. Considering Equation 17, a smaller voltage input requires a larger gain to achieve the same voltage input to the PZT actuators.

3.4. Validation of robot manipulator and link structure model

Prior to the validation of the combined model of the robot manipulator and the link structure, the kinematic model of the robot manipulator was compared with experimental data recorded by the KUKA$^©$ Sunrise Workbench (KSW). A helix was chosen to validate the prediction of the end effector position in Cartesian coordinates respective to the world frame of the robot manipulator, utilising three dimensions for comparison. The KSW was used to programme the end effector route, and record the joint angles at each way-point. These joint angles were then entered into the analytical model, and the Cartesian coordinates at each point were returned for comparison.
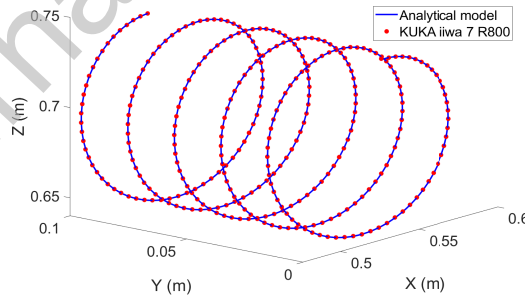

Figure 14: Comparison between the analytical model and the experimental results of the robot manipulator's end effector coordinates.

From Figure 14, the coordinates obtained from the model and the robot arm can be perceived to be a very close match. The average percentage error for each axis (x, y, z) was calculated to be 0.0107%, 0.0153% and 0.0067%,

respectively, which confirms that the model is a good approximation. However, in the case where the link structure is mounted upon the robot manipulator the model may not provide an accurate prediction of the end effector position due to the influence of the link structure upon the manipulator. Thus, to determine whether the kinematic model of the manipulator and the analytical model of the link structure/control system should be coupled, a further validation of the robot manipulator model was conducted. The experimental results were obtained whilst the robot was set to excite the mounted link structure through a series of frequencies, reducing the number of points for a better comparison. The corresponding joint angles from these points were obtained from the KSW, and used as an input into the analytical model as previously.
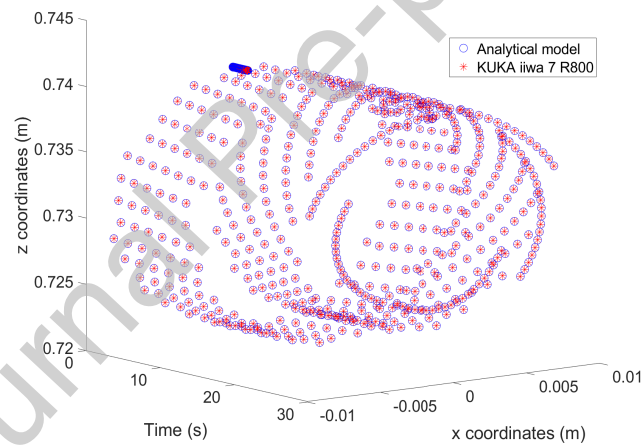

Figure 15: A comparison of the calculated end effector position from the analytical model and the end effector position retrieved from the experimental studies.

From Figure 15 it can be observed that there is little error between the experimental and predicted coordinates, as well as the time at which these points were reached. The average percentage error for each axis (x, y, z) was calculated to be 0.0042%, $6.88 \times 10^{-8}\%$ and $9.68 \times 10^{-7}\%$, respectively. With the prediction of the end effector position negating the link structure, there is

31

still very little error when compared to the experimental results in which the link structure was included. Thus, in order to predict the transverse motion of the link structure it is possible to utilise the end effector motion as an input into the analytical model of the link structure/control system.
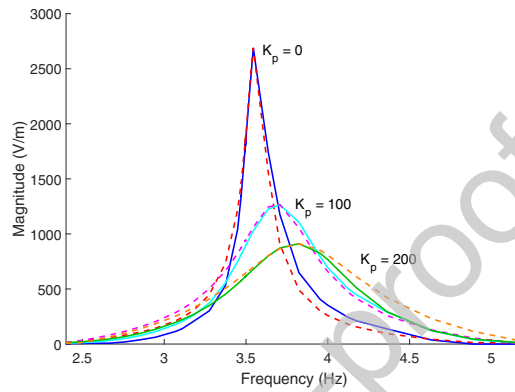

Figure 16: The response of the system against the frequency of excitation for three cases of K_p, for the experimental results (solid lines) and the analytical results (dashed lines).

Figure 16 shows the comparison of the analytical data from the link structure/control model, for three cases of control gain across the frequency range of 1.5 Hz to 6.75 Hz. The response in this case is the voltage output from the PZT sensors divided by the base displacement. Increasing the gain values proves to reduce the amplitude of the response as well as increase the natural frequency. When considering the voltage response of those frequencies immediately surrounding 3.59 Hz from the experimental results (solid lines) it is clear to see that the RPi system is highly effective. Although the proportionality of the voltage output to the displacement at the free end of the beam was proven not to be constant, it was proven to follow the same trend. With this fact it can be safely assumed from the decrease of voltage across the frequency range that the displacement experienced at the free end and thus throughout the link is also decreasing.

The analytical model required some slight adjustments from that used in Figure 9. Noise was present in the experimental readings, which required the

32

exchange of the resistance values R_2 and R_3 in Figure 4 from 10 $M\Omega$ to 1 $M\Omega$. However, even with this exchange, the smaller voltage readings affected by this noise required removal. These alterations were reflected in the analytical model, where the lower voltages were removed and the resistance and capacitance of the circuit adjusted to: $R_{lps} = 4.8$ and $C_{ps} = 0.0033$. As with the previous validation of the analytical model (Figure 9) the influence of the control system on the link's stiffness requires an additional factor in terms of the previously mentioned variable γ_v. With these justifiable alterations to the analytical model, it yielded accurate predictions of the experimental results for all three values of gain in terms of damping and natural frequency. This supports the hypothesis that the influence of the link on the robot manipulator need not be considered, as this interaction was not included in the model, yet closely matching results were obtained.

4. Conclusions

This research sought to design, test and analyse a lightweight, inexpensive control system suitable for use in a variety of applications to attenuate unwanted vibrations in a flexible link. This research realised that a potential application lies in exploration and search and rescue missions in which a robot manipulator was mounted on a drone or rover. A long slender robot link acting as a camera armature would be necessary in such missions where the camera is required to explore small areas. Thus, lending to the necessity for an AVC system as the geometry of the link renders it more likely to experience nuisance vibrations. The KUKA$^\copyright$ iiwa 7 R800 manipulator was chosen to test the system as a parallel to the suggested application. All chosen components of the control system were lightweight and inexpensive to ensure suitability for use in conjunction with a drone. The restrictions of the mass and cost of the components raised concerns regarding the performance of the control system, as the restrictions led to a certain level of compromise with respect to the processing capabilities. The system utilised a proportional controller in an effort to reduce the strain on

the processing power of the SBC. However, whilst developing and analytical model of the structure/system it was realised that an application of proportional control to the voltage output of the PZT sensors had the potential to render results akin to a proportional-derivative controller.

These concerns were addressed with a series of experiments, and the data from these was compared with predictions obtained from the analytical models of the robot manipulator and link structure to validate the models. In all these experiments the analytical models were found to be an accurate prediction of both the robot manipulator and the link structure, leading to the models being more than suitable for use in the prognosis of the response of the system. The experimental results were akin to proportional-derivative control being employed, where the weighting of these components was directly affected by the capacitance and the resistance of the system. Thus, lending that the system be suitable for an array of applications where in which one particular type of performance is considered more favourable (leaning towards either more proportional or derivative control). The performance of the designed control system was compared with that of a purpose-built control system. From these results it may be concluded that the two systems have a similar level of performance for the application of vibration suppression, lending to the potential for the designed control system being a proven appropriate solution to applications where cost and mass are restricted. Finally, it was proven that the kinematic model of the robot manipulator need not be coupled with the analytical models of the link structure and control system. The motion of the manipulator's end effector acquired experimentally was compared with data obtained from the respective analytical model. Whilst the experimental data attained with the link mounted, the model did not account for the additional link. With very little error observed between these two data sets it may be concluded that the link has negligible inertial effect on the robot manipulator utilised within the experimental studies.

34

Acknowledgements

References

[1] B. N. Agrawal, K. E. Treanor, Shape control of a beam using piezoelectric actuators, Smart Materials and Structures 8 (6) (1999) 729. `doi:https://doi.org/10.1088/0964-1726/8/6/303`.

[2] D. Karagiannis, V. Radisavljevic-Gajic, Sliding mode boundary control for vibration suppression in a pinned-pinned euler–bernoulli beam with disturbances, Journal of Vibration and Control 24 (6) (2018) 1109–1122. `doi:https://doi.org/10.1177/1077546316658578`.

[3] J. Yang, L. Jiang, D. C. Chen, Dynamic modelling and control of a rotating euler–bernoulli beam, Journal of sound and vibration 274 (3-5) (2004) 863–875. `doi:https://doi.org/10.1016/S0022-460X(03)00611-4`.

[4] A. Nikkhoo, Investigating the behavior of smart thin beams with piezoelectric actuators under dynamic loads, Mechanical Systems and Signal Processing 45 (2) (2014) 513–530. `doi:https://doi.org/10.1016/j.ymssp.2013.11.003`.

[5] P. Gaudenzi, R. Carbonaro, E. Benzi, Control of beam vibrations by means of piezoelectric devices: theory and experiments, Composite structures 50 (4) (2000) 373–379. `doi:https://doi.org/10.1016/S0263-8223(00)00114-8`.

[6] X. He, T. Ng, S. Sivashanker, K. Liew, Active control of fgm plates with integrated piezoelectric sensors and actuators, International journal of Solids and Structures 38 (9) (2001) 1641–1655. `doi:https://doi.org/10.1016/S0020-7683(00)00050-0`.

[7] Z.-c. Qiu, X.-m. Zhang, H.-x. Wu, H.-h. Zhang, Optimal placement and active vibration control for piezoelectric smart flexible cantilever plate, Journal of Sound and Vibration 301 (3-5) (2007) 521–543. doi:https://doi.org/10.1016/j.jsv.2006.10.018.

[8] K. Khorshidi, E. Rezaei, A. Ghadimi, M. Pagoli, Active vibration control of circular plates coupled with piezoelectric layers excited by plane sound wave, Applied Mathematical Modelling 39 (3-4) (2015) 1217–1228.

[9] Y. Dong, Y. Li, X. Li, J. Yang, Active control of dynamic behaviors of graded graphene reinforced cylindrical shells with piezoelectric actuator/sensor layers, Applied Mathematical Modelling 82 (2020) 252–270.

[10] F. dellIsola, C. Maurini, M. Porfiri, Passive damping of beam vibrations through distributed electric networks and piezoelectric transducers: prototype design and experimental validation, Smart Materials and Structures 13 (2) (2004) 299.

[11] D. Sun, J. K. Mills, J. Shan, S. Tso, A pzt actuator control of a single-link flexible manipulator based on linear velocity feedback and actuator placement, Mechatronics 14 (4) (2004) 381–401. doi:https://doi.org/10.1016/S0957-4158(03)00066-7.

[12] O. Garcia-Perez, G. Silva-Navarro, J. Peza-Solis, Flexible-link robots with combined trajectory tracking and vibration control, Applied Mathematical Modelling 70 (2019) 285–298.

[13] H.-C. Shin, S.-B. Choi, Position control of a two-link flexible manipulator featuring piezoelectric actuators and sensors, Mechatronics 11 (6) (2001) 707–729. doi:https://doi.org/10.1016/S0957-4158(00)00045-3.

[14] Z.-c. Qiu, C. Li, X.-m. Zhang, Experimental study on active vibration control for a kind of two-link flexible manipulator, Mechanical Systems and Signal Processing 118 (2019) 623–644. doi:https://doi.org/10.1016/j.ymssp.2018.09.001.

[15] J.-S. Oh, Y.-M. Han, S.-B. Choi, Vibration control of a camera mount system for an unmanned aerial vehicle using piezostack actuators, Smart materials and structures 20 (8) (2011) 085020.

[16] T. Sales, D. Rade, L. De Souza, Passive vibration control of flexible spacecraft using shunted piezoelectric transducers, Aerospace Science and Technology 29 (1) (2013) 403–412.

[17] M. Abdollahpouri, G. Takács, B. Rohal'-Ilkiv, Real-time moving horizon estimation for a vibrating active cantilever, Mechanical Systems and Signal Processing 86 (2017) 1–15. doi:https://doi.org/10.1016/j.ymssp.2016.09.028.

[18] X. Weber, L. Cuvillon, J. Gangloff, Active vibration canceling of a cable-driven parallel robot using reaction wheels, in: 2014 IEEE/RSJ International Conference on Intelligent Robots and Systems, IEEE, 2014, pp. 1724–1729. doi:https://doi.org/10.1109/iros.2014.6942787.

[19] M. A. Mahmud, K. Bates, T. Wood, A. Abdelgawad, K. Yelamarthi, A complete internet of things (iot) platform for structural health monitoring (shm), in: 2018 IEEE 4th World Forum on Internet of Things (WF-IoT), IEEE, 2018, pp. 275–279. doi:https://doi.org/10.1109/wf-iot.2018.8355094.

[20] B. Chomette, A. Mamou-Mani, Modal control based on direct modal parameters estimation, Journal of Vibration and Control 24 (12) (2018) 2389–2399. doi:https://doi.org/10.1177/1077546317726615.

[21] Y. Zhang, H. Lu, D. T. Pham, Y. Wang, M. Qu, J. Lim, S. Su, Peg–hole disassembly using active compliance, Royal Society open science 6 (8) (2019) 190476. doi:https://doi.org/10.1098/rsos.190476.

[22] I. Kuhlemann, A. Schweikard, P. Jauer, F. Ernst, Robust inverse kinematics by configuration control for redundant manipulators with seven dof, in: 2016 2nd International Conference on Control, Automation and

Robotics (ICCAR), IEEE, 2016, pp. 49–55. `doi:https://doi.org/10.1109/iccar.2016.7486697`.

[23] S. Li, Z. Wang, Q. Zhang, F. Han, Solving inverse kinematics model for 7-dof robot arms based on space vector, in: 2018 International Conference on Control and Robots (ICCR), IEEE, 2018, pp. 1–5. `doi:https://doi.org/10.1109/iccr.2018.8534498`.

[24] S. Starke, N. Hendrich, D. Krupke, J. Zhang, Evolutionary multi-objective inverse kinematics on highly articulated and humanoid robots, in: 2017 IEEE/RSJ International Conference on Intelligent Robots and Systems (IROS), IEEE, 2017, pp. 6959–6966. `doi:https://doi.org/10.1109/iros.2017.8206620`.

[25] P. I. Corke, A simple and systematic approach to assigning denavit–hartenberg parameters, IEEE transactions on robotics 23 (3) (2007) 590–594. `doi:https://doi.org/10.1109/tro.2007.896765`.

[26] C. Faria, F. Ferreira, W. Erlhagen, S. Monteiro, E. Bicho, Position-based kinematics for 7-dof serial manipulators with global configuration control, joint limit and singularity avoidance, Mechanism and Machine Theory 121 (2018) 317–334. `doi:https://doi.org/10.1016/j.mechmachtheory.2017.10.025`.

[27] A. Izadbakhsh, Closed-form dynamic model of puma 560 robot arm, in: 2009 4th International Conference on Autonomous Robots and Agents, IEEE, 2009, pp. 675–680. `doi:https://doi.org/10.1109/icara.2000.4803940`.

[28] G. Gao, G. Sun, J. Na, Y. Guo, X. Wu, Structural parameter identification for 6 dof industrial robots, Mechanical Systems and Signal Processing 113 (2018) 145–155. `doi:https://doi.org/10.1016/j.ymssp.2017.08.011`.

[29] D. Williams, H. Haddad Khodaparast, S. Jiffri, C. Yang, Active vibration control using piezoelectric actuators employing practical components,

Journal of Vibration and Control 25 (21-22) (2019) 2784–2798. doi:https://doi.org/10.1177/1077546319870933.

[30] A. Erturk, D. J. Inman, Piezoelectric energy harvesting, John Wiley & Sons, 2011.

[31] Lbr iiwa (2016).
URL https://www.kuka.com/en-gb/products/robotics-systems/industrial-robots/lbr-iiwa

[32] Macro fibre composite - mfc (2017).
URL https://www.smart-material.com/media/Datasheets/MFC_V2.3-Web-full-brochure.pdf

[33] The online materials information resource (2007).
URL http://www.matweb.com